Taylor & Francis
Taylor & Francis Group

Vehicle System Dynamics
International Journal of Vehicle Mechanics and Mobility

ISSN: (Print) (Online) Journal homepage: https://www.tandfonline.com/loi/nvsd20

Investigating nonlinear dynamic properties of a swing arm rubber joint and their effects on the dynamic behavior of high-speed trains

Xiangwang Chen, Longjiang Shen & Yuan Yao

To cite this article: Xiangwang Chen, Longjiang Shen & Yuan Yao (02 Feb 2024): Investigating nonlinear dynamic properties of a swing arm rubber joint and their effects on the dynamic behavior of high-speed trains, Vehicle System Dynamics, DOI: 10.1080/00423114.2024.2312914

To link to this article: https://doi.org/10.1080/00423114.2024.2312914

Published online: 02 Feb 2024.

VEHICLE SYSTEM DYNAMICS
https://doi.org/10.1080/00423114.2024.2312914

Investigating nonlinear dynamic properties of a swing arm rubber joint and their effects on the dynamic behavior of high-speed trains

Xiangwang Chen[a], Longjiang Shen[b] and Yuan Yao[a]

[a]State Key Laboratory of Rail Transit Vehicle System, Southwest Jiaotong University, Chengdu, People's Republic of China; [b]Bogie R&D Department, CRRC Zhuzhou Electric Locomotive Co., Ltd., Zhuzhou, People's Republic of China

ABSTRACT

The rubber joints mounted on swing arms provide the main part of the yaw stiffness for wheelsets and thus have a significant influence on the dynamic behaviour of railway vehicles. However, their nonlinear dynamic properties concerning the frequency, amplitude, and temperature were not fully considered in previous studies, most of which adopt simple models such as the Kelvin–Voigt model to represent rubber components. This study aims to investigate the radial nonlinear properties of swing arm rubber joints under various conditions and assess their effects on the dynamic performance of high-speed trains. A nonlinear rubber spring model which combines the fractional derivative Zener model with Berg's friction model is established. To achieve a better fit to the measurements of a swing arm rubber joint, an optimisation-based method is employed to identify the model parameters. The viscous and frictional effects of the rubber joint are compared at different frequencies, amplitudes, and temperatures, by determining the predominant element of the nonlinear model. Additionally, the nonlinear rubber spring model is integrated into a high-speed vehicle dynamic model to investigate the effects of the nonlinear properties of swing arm rubber joints on the vehicle dynamic behaviour through the MATLAB/SIMPACK co-simulation method.

ARTICLE HISTORY
Received 17 August 2023
Revised 19 January 2024
Accepted 25 January 2024

KEYWORDS
Swing arm rubber joint; dynamic property; fractional derivative; high-speed train; vehicle dynamics

1. Introduction

Rubber components are widely used in railway vehicles, serving as crucial elements in primary and secondary suspension systems, such as the rubber joint mounted on axle box swing arms, damper elastic joint, bump stop, etc. Achieving excellent running dynamics of high-speed trains requires suitable matching of parameters for these rubber components, especially the swing arm rubber joint (SARJ). It connects axle boxes to bogie frames and provides the main part of the yaw stiffness for wheelsets, having a significant influence on the running stability, curving performance, and ride comfort of vehicles [1]. Therefore, it is essential to investigate the nonlinear dynamic properties of SARJs and determine

CONTACT Yuan Yao yyuan8848@163.com

their effects on the running dynamics of high-speed trains. Since the stiffness and damping of rubber components strongly depend on the material property, working state and ambient temperature, etc., they demonstrate noticeable nonlinear properties, including frequency-dependent, amplitude-dependent, and temperature-dependent properties. This poses a challenge to developing an accurate mechanical model of rubber components for vehicle dynamics simulations and designing SARJs with desired dynamic behaviour [2].

The Kelvin–Voigt (KV) model, where a linear spring is coupled in parallel with a viscous dashpot, is the most used model to describe the behaviour of rubber components in vehicle dynamics simulations. However, it strongly overestimates both stiffness and damping at higher frequencies due to the presence of the viscous dashpot [3]. In order to improve the modelling accuracy, Sun et al. [4] and Luo et al. [5] corrected the KV model by changing the spring and dashpot coefficients with the vibration amplitude and frequency, whereas the parameter identification was complex. Including more chains of springs and dashpots can improve the representation accuracy regarding the frequency dependence, such as the three-parameter Maxwell model (also called the Zener model) [6] and generalised Maxwell model [7,8], which adopts one or more chains composed of a spring in series with a dashpot. However, as these models include more elements of springs and dashpots, the complexity and parameter numbers increase dramatically, as well as the difficulty of adjusting constant parameters from measurements. More recently, fractional derivatives have been used to model viscoelastic behaviour [9]. Compared to the model with integer order derivatives, they require fewer parameters but obtain an excellent description of the frequency-dependent property over a wide frequency range. Sjoberg and Kari [10], Sedlaczek et al. [11], and Shi and Wu [12] adopted a three-parameter fractional derivative model to represent the frequency dependence of rubber isolators. Yang et al. [13] and Wei et al. [14] analysed the high-speed vehicle-slab track coupled vibration by employing a four-parameter fractional derivative model to describe the behaviour of rail pads.

In addition to the frequency dependence, including carbon-black or other fillers in rubber components results in friction-like behaviour, and their dynamic properties are closely correlated with the excitation amplitude. Incorporating a spring in series with a Coulomb friction element can exhibit the amplitude-dependent behaviour, but more chains are required to achieve smoother characteristics [15,16]. Berg [17,18] proposed a friction model which captures the amplitude dependence with only two parameters. It can reproduce smooth force-displacement hysteresis loops with fewer parameters than Coulomb friction elements and thus is widely adopted in rubber modelling. Additionally, the dynamic properties of rubber materials are sensitive to the ambient temperature. Yang [19] and Wei et al. [14] measured the dynamic properties of rubber components at different temperatures and modelled the temperature dependence based on Time-Temperature Superposition and Williams-Landel-Ferry formula. In addition to the above overlay methods, where the viscoelastic and plastic behaviour (i.e. frequency- and amplitude-dependent behaviour) are represented separately, some rubber models represent the frequency and amplitude dependence in a coupling manner. Luo et al. [20] proposed a nonlinear rubber spring model composed of nonlinear spring and dashpot elements and introduced five additional parameters to improve the model performance. Sohn et al. [21] and Dai et al. [22] presented hybrid neural network models to describe the nonlinear properties of rubber components. However, these models require a large number of measurement results to train neural networks, and their physical meanings are not clear.

Due to its crucial role in suspension systems, many studies focus on the influence of SARJ parameters on vehicle dynamics. Shi et al. [23] and Guan et al. [24] investigated the influence of primary longitudinal stiffness on the linear stability of railway vehicles. Wu et al. [25] and Polach et al. [26] studied the relationship between the type of bogie hunting bifurcation and stiffness of primary suspensions. Song et al. [27] measured the static longitudinal stiffness of SARJs that served for a long time and analysed the stiffness influence on the dynamic performance of a high-speed train considering the variation of wheel and rail profiles. To address the trade-off between running stability and curving performance for a vehicle, Lewis et al. [28] and Qu et al. [29] incorporated a hydraulic-damping-integrated bush into the swing arm to realise the desired frequency-dependent primary yaw stiffness. The aforementioned studies indicate that the dynamic behaviour of SARJs, especially in the radial direction, significantly influences the running dynamics of railway vehicles. However, previous studies mostly adopted a simple model such as the KV model to describe their stiffness and damping properties in the vehicle dynamics analysis, which leads to significant deviations from the real properties under distinct scenarios. Therefore, it is necessary to assess the deviation of vehicle dynamic responses when adopting a simple KV model. Moreover, although the dynamic properties of SARJs have been tested at different excitation frequencies, amplitudes and temperatures [12,20,22], their effects on vehicle dynamic behaviour are not fully investigated.

Given that the primary yaw stiffness has a more significant influence on running dynamics of high-speed trains, this study focuses on the radial dynamic properties of SARJs. A nonlinear rubber spring model that considers the frequency, amplitude and temperature dependence is established, and the basic theories about it are expounded. In order to obtain a better fit to measurements, an optimisation-based parameter identification method is employed to determine six model parameters. Next, the nonlinear dynamic behaviour of a SARJ is extensively investigated using the presented rubber spring model, with the emphasis put on the comparison between the viscous and frictional effects under various scenarios. Finally, to assess the effects of the SARJ's nonlinear properties on vehicle dynamic behaviour, the presented rubber model is integrated into a high-speed train dynamic model through MATLAB/SIMPACK co-simulation. By determining the effects of the frequency, amplitude and temperature dependence, it is possible to point out the optimised direction of the dynamic behaviour of SARJs.

2. Theoretical models for the nonlinear dynamic properties

The presented nonlinear model for rubber components is one-dimensional and consists of three independent branches. The total force can be written as [17]

$$F = F_{\mathrm{e}} + F_{\mathrm{v}} + F_{\mathrm{f}} \tag{1}$$

where the elastic force F_{e} represents the static behaviour of rubber components, the viscous force F_{v} accounts for the frequency dependence, and the friction force F_{f} considers the amplitude dependence.

Due to its ability to capture the frequency dependence over a wide frequency range with fewer parameters, the fractional derivative model is used to represent the viscoelastic behaviour. The common fractional derivative models include the fractional derivative Kelvin–Voigt model [10–12], fractional derivative Zener model [30] and five-parameter fractional derivative model [31]. As the model parameters increase, they can describe more complex viscoelastic behaviour of rubber components. In this study, the fractional derivative Zener model with four undetermined parameters is adopted, since it is able to effectively represent the viscoelastic behaviour at sufficiently high frequencies for the rubber components in vehicle-track systems [13,14]. Additionally, Berg's friction model [17,18] with two undetermined parameters is used to achieve a smooth fit to measured frictional hysteresis curves. As a result, the nonlinear model that combines the fractional derivative Zener model with Berg's friction model has a total of six parameters, making it an attractive tool for applications in vehicle dynamics simulations.

After obtaining the output force of rubber components subjected to a harmonic displacement excitation with the amplitude of x_0, the dynamic stiffness K_d and normalised damping D are generally used to characterise their dynamic properties. They are calculated from the force-displacement hysteresis loop and expressed as:

$$K_\mathrm{dyn} = \frac{F_0}{x_0} \tag{2}$$

$$D = \sin\delta = \frac{E}{\pi F_0 x_0} \tag{3}$$

where F_0 is the amplitude of the output force, δ is the loss angle, and E represents the energy loss for each cycle and is calculated by the surrounded area of the hysteresis loop.

2.1. Fractional derivative Zener model

The constitutive equation for the fractional derivative Zener model in time domain is formulated as [30]:

$$F_\mathrm{ev}(t) + \tau^\alpha \frac{\mathrm{d}^\alpha}{\mathrm{d}t^\alpha} F_\mathrm{ev}(t) = K_0 x(t) + K_\infty \tau^\alpha \frac{\mathrm{d}^\alpha}{\mathrm{d}t^\alpha} x(t) \tag{4}$$

where the viscoelastic force F_ev is the sum of F_e and F_v, x represents the displacement, K_0 and K_∞ are the static stiffness and high-frequency limit value of the storage stiffness, respectively, τ denotes the relaxation time, α is an arbitrary order of the time derivative and $0 < \alpha \leq 1$. When $\alpha = 1$, the model degenerates into the ordinary Zener model.

As a common representation of fractional derivatives, the discrete Grunwald definition is suitable for numerical implementation [32]. The fractional derivative based on this definition can be expressed as:

$$\frac{\mathrm{d}^\alpha x(t)}{\mathrm{d}t^\alpha} = \lim_{N\to\infty} \left(\frac{t}{N}\right)^{-\alpha} \sum_{i=0}^{N-1} A_{i+1} x\left(t - i\frac{t}{N}\right) \tag{5}$$

where the Grunwald coefficient A_{i+1} satisfies the following recurrence formula with $A_1 = 1$:

$$A_{i+1} = \frac{\Gamma(i-\alpha)}{\Gamma(-\alpha)\Gamma(i+1)} = \left(1 - \frac{\alpha+1}{i}\right) A_i \tag{6}$$

where $\Gamma(\cdot)$ denotes the gamma function. Equation (5) suggests that the fractional operator has a typical non-local characteristic, requiring the previous time history to calculate the present value of the fractional derivative. This is consistent with the memory characteristic of rubber components. Moreover, as indicated in Equation (6), the influence of the previous time history on calculating the present fractional derivative diminishes strictly, and A_{i+1} tends to zero with increasing i. Furthermore, a larger value of α results in faster convergence of A_{i+1}. Therefore, only the latest part of the time history needs to be considered when evaluating the fractional derivative. This feature avoids storing the whole time history and significantly reduces the computational effort in dynamic simulations.

A truncation form of Equation (5) with the finite difference approximation is given by [32]:

$$\frac{\mathrm{d}^\alpha x(t)}{\mathrm{d}t^\alpha} \approx h^{-\alpha} \sum_{i=0}^{N_t-1} A_{i+1} x(t-ih) \tag{7}$$

where h refers to the numerical time step, and N_t is the truncation number of previous steps that are used to calculate the present fractional derivative value. Similarly, the fractional derivative of the viscoelastic force can be written as:

$$\frac{\mathrm{d}^\alpha F_{\mathrm{ev}}(t)}{\mathrm{d}t^\alpha} \approx h^{-\alpha} \sum_{i=0}^{N_t-1} A_{i+1} F_{\mathrm{ev}}(t-ih) \tag{8}$$

By substituting Equations (7) and (8) into (4), $F_{\mathrm{ev}}(t)$ can be further obtained as follows:

$$F_{\mathrm{ev}}(t) = \frac{K_0 x(t) + K_\infty \tau^\alpha h^{-\alpha} \sum_{i=0}^{N_t-1} A_{i+1} x(t-ih) - \tau^\alpha h^{-\alpha} \sum_{i=1}^{N_t-1} A_{i+1} F_{\mathrm{ev}}(t-ih)}{1+\tau^\alpha h^{-\alpha}} \tag{9}$$

The viscous force $F_{\mathrm{v}}(t)$ accounting for the frequency dependence can be obtained by subtracting the elastic force:

$$F_{\mathrm{v}}(t) = F_{\mathrm{ev}}(t) - K_0 x(t) \tag{10}$$

According to Equation (4), the complex stiffness for the fractional derivative Zener model can be derived analytically through the Fourier transform:

$$K_{\mathrm{ev}}(\omega) = \frac{F_{\mathrm{ev}}(\omega)}{x(\omega)} = K_{\mathrm{evS}}(\omega) + jK_{\mathrm{evL}}(\omega) = \frac{K_0 + K_\infty (j\omega\tau)^\alpha}{1+(j\omega\tau)^\alpha} \tag{11}$$

where ω is the circular frequency, j is the imaginary unit, K_{evS} and K_{evL} are the storage stiffness and loss stiffness, respectively. Given $j^\alpha = \cos(\alpha\pi/2) + j\sin(\alpha\pi/2)$, K_{evS} and K_{evL} can be written as:

$$K_{\mathrm{evS}}(\omega) = \frac{K_0 + (K_0 + K_\infty)\tau^\alpha\omega^\alpha \cos\left(\frac{\alpha\pi}{2}\right) + K_\infty \tau^{2\alpha}\omega^{2\alpha}}{1+\tau^{2\alpha}\omega^{2\alpha} + 2\tau^\alpha\omega^\alpha \cos\left(\frac{\alpha\pi}{2}\right)} \tag{12}$$

$$K_{\mathrm{evL}}(\omega) = \frac{(K_\infty - K_0)\tau^\alpha\omega^\alpha \sin\left(\frac{\alpha\pi}{2}\right)}{1+\tau^{2\alpha}\omega^{2\alpha} + 2\tau^\alpha\omega^\alpha \cos\left(\frac{\alpha\pi}{2}\right)} \tag{13}$$

Equations (11)–(13) indicate that the dynamic properties relate to the excitation frequency and four parameters included in the fractional derivative model and are independent of the

Table 1. Model parameters identified at different temperatures.

	Fractional derivative Zener model				Berg's friction model	
Temperature (°C)	K_0 (kN/mm)	K_∞ (kN/mm)	τ (s)	α	x_2 (mm)	F_{fmax} (kN)
20	12.29	14.01	0.043	0.659	1.41	4.57
0	12.31	14.08	0.031	0.796	1.58	7.77
−20	12.82	17.98	0.018	0.864	1.09	6.18
−40	15.06	27.09	0.015	0.861	0.463	6.86

displacement amplitude. In addition, the complex stiffness for the discrete approximation of the fractional derivative model in Equation (9) is derived to investigate its accuracy:

$$K_{\mathrm{ev}}^* = \frac{K_0 + K_\infty \tau^\alpha h^{-\alpha} \sum_{k=0}^{N_t-1} A_{k+1}(\cos(kh\omega) - j\sin(kh\omega))}{1 + \tau^\alpha h^{-\alpha} \sum_{k=0}^{N_t-1} A_{k+1}(\cos(kh\omega) - j\sin(kh\omega))} \tag{14}$$

The discrete approximation facilitates the numerical calculation of fractional derivatives through the summation of the time history. However, its accuracy is closely related to the truncation number N_t of terms in the sum and time step h. Their effects on the results of the discrete approximation must be investigated to avoid reducing the accuracy in calculating the fractional derivative Zener model.

Figure 1 depicts the storage stiffness K_{evS} and loss stiffness K_{evL} obtained by the continuous definition in Equation (11) and the discrete approximation in Equation (14). The truncation number N_t and time step h are set to various values to investigate their effects on the calculation accuracy. The other parameters in the fractional derivative Zener model adopt the values identified at a temperature of 20°C, as listed in Table 1. Figure 1(a) shows the effects of h with $N_t = 400$. It is observed that h has a significant effect on calculating the dynamic properties, especially for the loss stiffness. Selecting a large time step such as $h = 1 \times 10^{-2}$ s can obtain a good fit to the actual value of the fractional derivative model at lower frequencies, while the calculation accuracy becomes poor as the frequency increases. On the other hand, continuously reducing h may also result in an unsatisfactory performance of the discrete approximation. When $h = 1 \times 10^{-4}$ s is selected, the calculation accuracy is poor at frequencies below 10 Hz, although it provides a better fit at higher frequencies. In this case, N_t must increase to cover a longer previous time history, which is essential to improve the calculation accuracy, especially at low frequencies. Selecting $h = 1 \times 10^{-3}$ s provides the best accuracy for the discrete approximation in the studied frequency range. Figure 1(b) displays the effects of N_t on the dynamic properties with $h = 1 \times 10^{-3}$ s. Its effects are evident at lower frequencies, where a smaller N_t results in an obvious deviation from the actual value.

In summary, the selection of N_t and h significantly affects the calculation results of the fractional derivative. Their combination should cover a sufficiently long time history composed of smaller time steps so as to capture detailed characteristics of previous signals, contributing to the accurate representation of the frequency dependence of rubber components. Meanwhile, the computational effort must be acceptable to make it possible to conduct vehicle dynamics simulations. In this study, calculating the fractional derivative Zener model employs $N_t = 200$ and $h = 1 \times 10^{-3}$ s, and then Equation (9) reads as

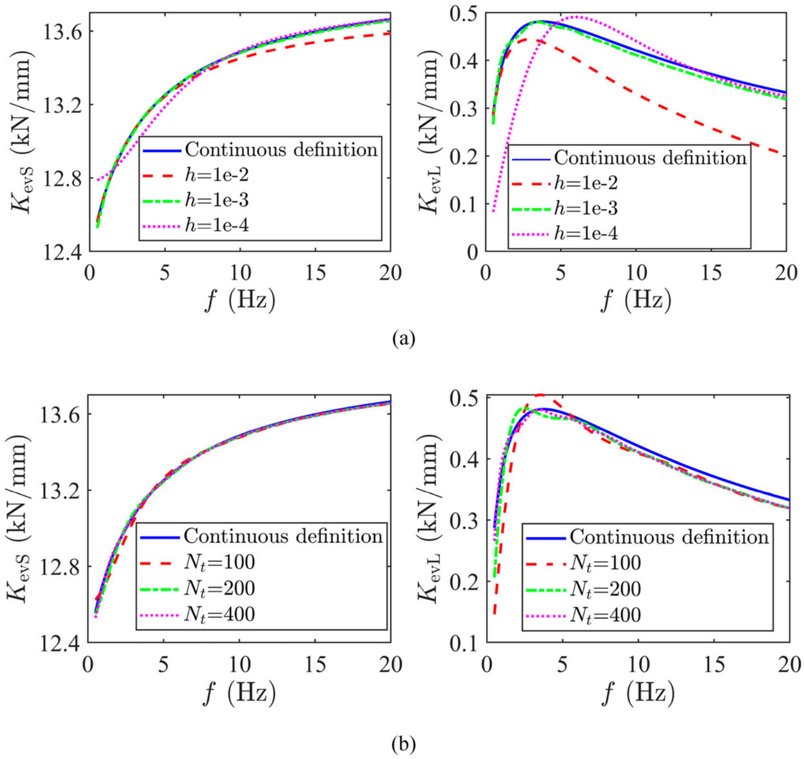

Figure 1. Influence of the parameter setting in the discrete approximation on frequency-dependent properties: (a) time step h; (b) truncation number N_t.

follows:

$$F_{ev}(t) = \begin{cases} \dfrac{K_0x(t)+K_\infty\tau^\alpha h^{-\alpha}\sum\limits_{i=0}^{N_t-1}A_{i+1}x(t-ih)-\tau^\alpha h^{-\alpha}\sum\limits_{i=1}^{N_t-1}A_{i+1}F_{ev}(t-ih)}{1+\tau^\alpha h^{-\alpha}} & \text{for } N_t \le 200 \\ \dfrac{K_0x(t)+K_\infty\tau^\alpha h^{-\alpha}\sum\limits_{i=0}^{199}A_{i+1}x(t-ih)-\tau^\alpha h^{-\alpha}\sum\limits_{i=1}^{199}A_{i+1}F_{ev}(t-ih)}{1+\tau^\alpha h^{-\alpha}} & \text{for } N_t > 200 \end{cases} \quad (15)$$

2.2. Berg's smooth friction model

In Berg's friction model, the friction force F_f depends not only on the displacement x over the element, but also on a reference state in the force-displacement hysteresis curve. The friction force can be expressed as [17]:

$$F_f = \begin{cases} F_{fs} & \text{for } x = x_s \\ F_{fs} + \frac{x-x_s}{x_2(1-\mu)+(x-x_s)}(F_{fmax} - F_{fs}) & \text{for } x > x_s \\ F_{fs} + \frac{x-x_s}{x_2(1+\mu)-(x-x_s)}(F_{fmax} + F_{fs}) & \text{for } x < x_s \end{cases} \quad (16)$$

where $\mu = F_{fs}/F_{fmax}$ is an auxiliary quantity ranging from -1 to 1, F_{fs} and x_s refer to the force and displacement of the reference state and will be updated once the velocity direction changes. The two parameters that need to be determined are F_{fmax} and x_2. F_{fmax} represents the maximum friction force the friction element can provide. x_2 is the displacement

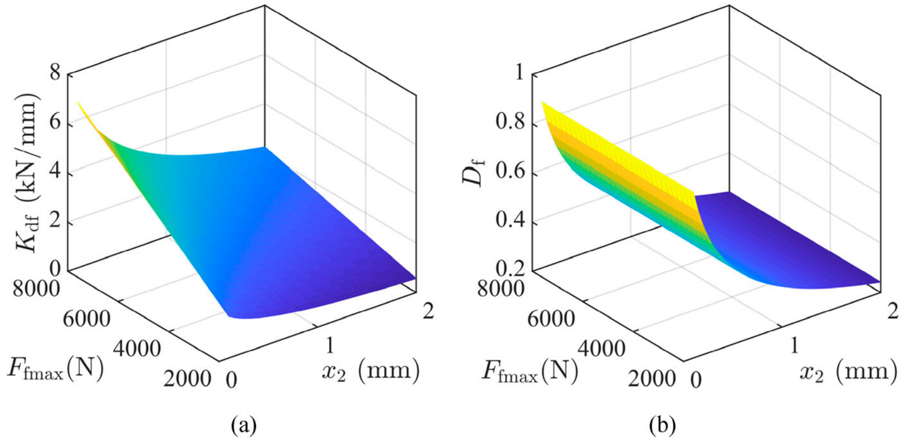

Figure 2. Influence of the friction model parameters on dynamic properties.

required to reach half of the maximum friction force after monotonically increasing from $(x_s, F_{fs}) = (0, 0)$, and a small value of x_2 provides a steep force increase and high frictional stiffness.

The friction force develops nonlinearly with displacement and reaches a steady-state force-displacement loop after almost three cycles. When subjected to a harmonic displacement excitation with the amplitude of x_0, the steady-state force amplitude F_{f0} and energy loss per cycle E_f for the friction model are given by [17]:

$$F_{f0} = \frac{F_{fmax}}{2x_2}\left(\sqrt{x_2^2 + x_0^2 + 6x_2x_0} - x_2 - x_0\right) \tag{17}$$

$$E_f = 2F_{fmax}\left(2x_0 - x_2(1+\mu_0)^2 \ln \frac{x_2(1+\mu_0) + 2x_0}{x_2(1+\mu_0)}\right) \tag{18}$$

Here $\mu_0 = F_{f0}/F_{fmax}$. Referring to the definitions in Equations (2) and (3), the dynamic stiffness K_{df} and damping D_f for the friction model are obtained as follows:

$$K_{df} = \frac{F_{f0}}{x_0} = \frac{F_{fmax}}{2x_2x_0}\left(\sqrt{x_2^2 + x_0^2 + 6x_2x_0} - x_2 - x_0\right) \tag{19}$$

$$D_f = \frac{E_f}{\pi F_{f0}x_0} = \frac{2}{\pi\mu_0x_0}\left(2x_0 - x_2(1+\mu_0)^2 \ln \frac{x_2(1+\mu_0) + 2x_0}{x_2(1+\mu_0)}\right) \tag{20}$$

Equations (19) and (20) indicate that the dynamic properties K_{df} and D_f are only dependent on the displacement amplitude x_0 and friction model parameters F_{fmax} and x_2. The influences of the friction model parameters F_{fmax} and x_2 on K_{df} and D_f are illustrated in Figure 2. It can be observed that K_{df} increases with increasing F_{fmax} and decreasing x_2. Furthermore, K_{df} correlates with F_{fmax} linearly but demonstrates a more significant increase as x_2 decreases. D_f is unrelated to F_{fmax} but increases dramatically with decreasing x_2.

2.3. Total model behaviour

Based on Equations (19) and (20), the storage stiffness K_{fS} and loss stiffness K_{fL} in the friction branch can be written as follows:

$$K_{\mathrm{fS}} = K_{\mathrm{df}} \cos \delta_{\mathrm{f}} = K_{\mathrm{df}} \sqrt{1 - D_{\mathrm{f}}^2} \tag{21}$$

$$K_{\mathrm{fL}} = K_{\mathrm{df}} \sin \delta_{\mathrm{f}} = K_{\mathrm{df}} D_{\mathrm{f}} \tag{22}$$

where δ_{f} represents the loss angle in the friction element. Combining the dynamic properties of the friction element with those of the viscoelastic element, the total complex stiffness for the nonlinear rubber spring model is written as:

$$K_{\mathrm{dyn}} = K_{\mathrm{ev}} + K_{\mathrm{f}} = (K_{\mathrm{evS}} + K_{\mathrm{fS}}) + j(K_{\mathrm{evL}} + K_{\mathrm{fL}}) \tag{23}$$

The total dynamic stiffness is the modulus of the complex stiffness and is written as:

$$K_{\mathrm{dyn}} = |K_{\mathrm{dyn}}| = \sqrt{(K_{\mathrm{evS}} + K_{\mathrm{fS}})^2 + (K_{\mathrm{evL}} + K_{\mathrm{fL}})^2} \tag{24}$$

The elastic force does not lose energy during an oscillation, whereas both the viscous and friction forces contribute to the energy dissipation. The energy loss E_{v} per cycle for the viscous force is given by:

$$E_{\mathrm{v}} = \pi x_0 F_{\mathrm{v0}} \sin \delta_{\mathrm{v}} = \pi x_0^2 K_{\mathrm{evL}} \tag{25}$$

with F_{v0} the amplitude of the viscous force and δ_{v} the loss angle. The total energy loss E is the sum of E_{v} and E_{f}, and thus the damping D can be expressed as follows:

$$D = \frac{E}{\pi x_0^2 K_{\mathrm{dyn}}} \tag{26}$$

The equivalent viscous damping C_{eq} is also commonly used to represent the ability to dissipate energy. It is expressed as.

$$C_{\mathrm{eq}} = \frac{E}{\pi \omega x_0^2} \tag{27}$$

Equations (21)–(27) along with Equations (12), (13), (19), and (20) constitute the nonlinear mathematical model of rubber springs. Once the six model parameters are determined, this model enables the analysis of the dynamic properties under different excitation conditions.

3. Parameter identification

Typically, at least two types of measurements are required to determine the model parameters [12,17,18,33]. In the first step, the force-displacement curve measured under a large displacement and low frequency is used to obtain K_0, F_{fmax} and x_2. The excitation frequency must be sufficiently low, such as below 0.1 Hz, to eliminate the effect of the viscous

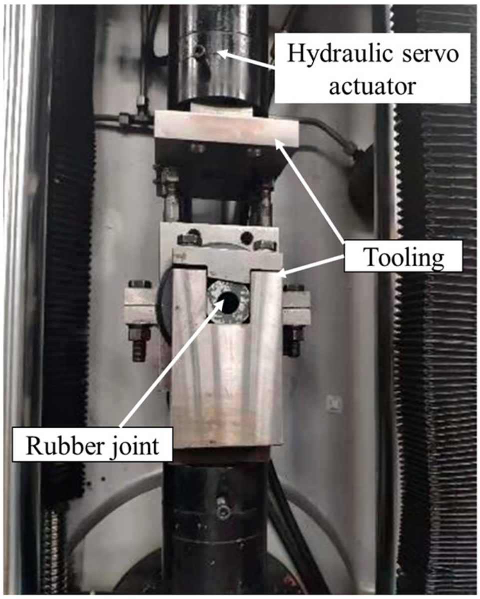

Figure 3. Experiment setup for the SARJ [34].

force, and then the three parameters can be read directly when the friction force is almost totally released at a sufficiently large displacement. The detailed schematic identification method can be found in Ref [18]. However, this method only can be applied to smooth measured curves, putting forward high requirements for conducting the experiments of rubber components. In the second step, the parameters in the viscous branch are identified at higher frequencies to achieve the best fit in a least-squared sense compared to measurements. In order to improve the efficiency of the parameter identification and utilise all experimental data measured under various amplitudes and frequencies, this study identifies all model parameters through an optimisation problem, which can achieve the best holistic fit to experimental results.

The radial dynamic properties of a SARJ used in high-speed trains have been tested by Dai [34]. Figure 3 shows the experiment setup for the SARJ. The test bench is equipped with an electro-hydraulic servo system that allows an accurate test at a higher frequency. The controlled sinusoidal excitation with different amplitudes and frequencies is adopted as the input, and the installed displacement sensor and force sensor measure the signals of deformation and force of the SARJ. In addition, the experimental test considers the influence of the temperature, which is essential for railway vehicles operating in low-temperature regions, such as North-eastern China. To investigate the dynamic properties at different temperatures, the SARJ is first adjusted in a temperature control box for no less than 24 h before performing the test.

Referring to the measurements presented in Ref [34], the performance of the proposed rubber spring model is examined. The SARJ typically experiences deformations of less than 2 mm with a working frequency below 10 Hz, mainly depending on the hunting motion of vehicles. Therefore, the measurements of dynamic stiffness and equivalent damping in the frequency range of 0.5-14 Hz with amplitudes of 0.5 and 1 mm are extracted from Ref [34] to identify the model parameters, and their corresponding errors are expressed as:

$$e_K = \frac{K^{\mathrm{s}}_{\mathrm{dyn}} - K^{\mathrm{m}}_{\mathrm{dyn}}}{K^{\mathrm{m}}_{\mathrm{dyn}}},\ e_C = \frac{C^{\mathrm{s}}_{\mathrm{eq}} - C^{\mathrm{m}}_{\mathrm{eq}}}{C^{\mathrm{m}}_{\mathrm{eq}}} \tag{28}$$

where $K^{\mathrm{s}}_{\mathrm{dyn}}$ and $C^{\mathrm{s}}_{\mathrm{eq}}$ represent the simulated results, and $K^{\mathrm{m}}_{\mathrm{dyn}}$ and $C^{\mathrm{m}}_{\mathrm{eq}}$ refer to the measurements. An optimisation function is then constructed as the weighted sum of squared errors:

$$F(x) = \sum_{i=1}^{N_A} \sum_{j=1}^{N_F} (w_K e^2_{Kij} + w_C e^2_{Cij}) \tag{29}$$

where $\mathbf{x}$ is a vector representing the model parameters, N_A and N_F are the number of amplitudes and frequencies of harmonic excitations, respectively, w_K and w_C represent weighting coefficients and can be determined according to the desired error tolerance for stiffness and damping. In this study, $w_K = 100$ and $w_C = 1$ are used for the stiffness and damping, respectively, since the damping effect is weak in SARJs, and higher accuracy is desired for the dynamic stiffness. The genetic algorithm is used to solve the optimisation problem, and the final optimisation results of the model parameters are presented in Table 1.

Figure 4 illustrates the measurements and simulated results for the dynamic properties of the SARJ. It is seen that the SARJ exhibits distinct frequency-, amplitude-, and temperature-dependent properties. Overall, as the frequency increases, the dynamic stiffness K_{dyn} increases, while the equivalent damping C_{eq} decreases. Additionally, K_{dyn} increases with decreasing amplitude, while C_{eq} is less sensitive to the amplitude. Note that the temperature significantly influences the dynamic properties. Both K_{dyn} and C_{eq} increase as the temperature decreases. Moreover, the frequency and amplitude dependence become more significant at lower temperatures. For instance, at a low temperature of −40°C, K_{dyn} increases by 43% as the frequency rises from 0.5 to 14 Hz with an amplitude of 0.5 mm, and it increases by 15% as the displacement amplitude decreases from 1 to 0.5 mm at a frequency of 14 Hz. Correspondingly, C_{eq} decreases by 89% and increases by 20%, respectively.

The simulated dynamic properties perfectly match the measurements, especially at a higher temperature. Although the model's accuracy deteriorates as the temperature decreases, the maximum error is 4% for the stiffness and 25% for the damping at −40 °C, meeting the requirements for engineering applications in vehicle dynamics simulations. It is important to note that establishing the nonlinear rubber model is based on the assumption that the viscous parameters are independent of the frictional parameters. However, as can be observed in Figure 4, the actual amplitude dependence becomes more pronounced with increasing frequency, especially at lower temperatures. This leads to the degradation in the model's performance at lower temperatures.

4. Nonlinear dynamic analysis

In this section, the presented model is simulated under various harmonic excitations to investigate the dynamic properties of the SARJ. Figure 5 compares the force-displacement hysteresis loops by applying harmonic displacement excitations with different amplitudes

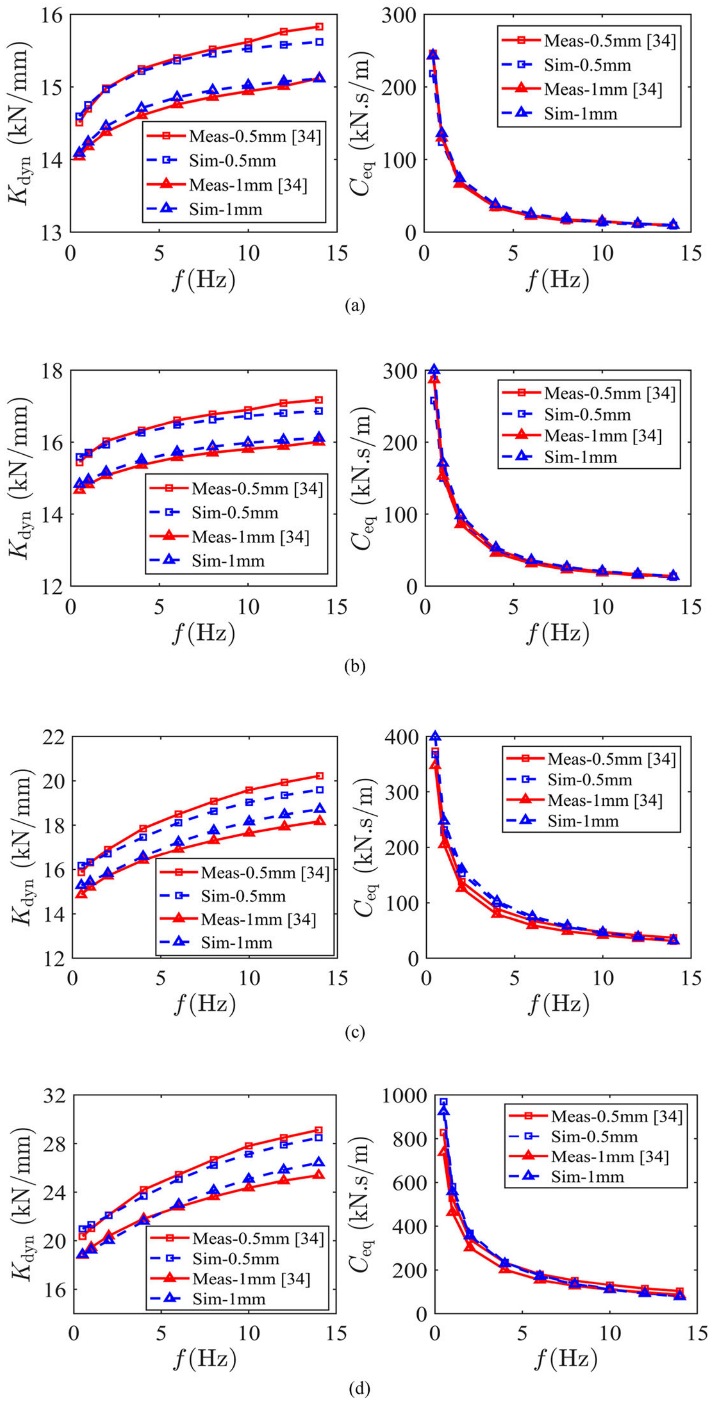

Figure 4. Dynamic properties of the presented nonlinear model compared to measurements at different temperature: (a) 20°C; (b) 0°C; (c) −20°C; (d) −40°C.

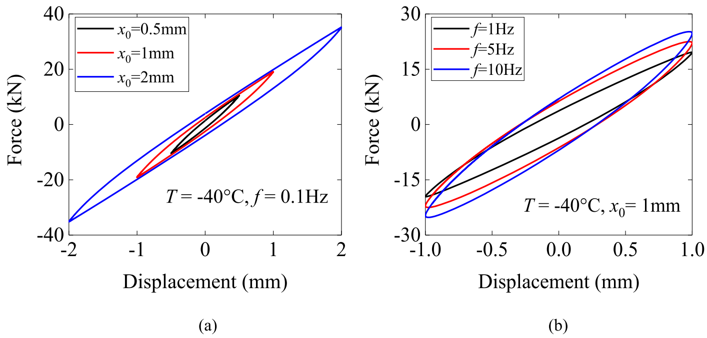

Figure 5. Predicted hysteresis loops for harmonic excitations with different amplitudes and frequencies: (a) amplitude dependence; (b) frequency dependence.

and frequencies at a temperature of $T = -40$ °C. The amplitude dependence is demonstrated in Figure 5(a), where the viscous force can be neglected as the frequency f is set to a quite low value of 0.1 Hz. Due to the frictional behaviour of the SARJ, the hysteresis loops exhibit sharp corners at the minimum and maximum displacements. In addition, as the displacement amplitude increases, the slope of the hysteresis loop, representing the dynamic stiffness of the SARJ, decreases, whereas the surrounded area increases, indicating that more energy is consumed per cycle. Figure 5(b) demonstrates the frequency dependence of the SARJ. The hysteresis loop tends to be elliptical in the presence of the viscous effect but remains somewhat peaked at the maximum and minimum displacements due to the frictional effect. With increasing frequency, both the slope of the loop and its surrounded area increase, indicating an increase in the dynamic stiffness and energy loss for the SARJ.

To investigate the influence of temperature on the frequency- and amplitude-dependent dynamic properties, the hysteresis loops for the viscous force F_v and friction force F_f are separately plotted in Figure 6(a), while the total force F is plotted in Figure 6(b). The excitation amplitude is 0.5 mm, and the frequency is 4 Hz. In Figure 6(a), it is evident that the slope and surrounded area for the viscous and frictional hysteresis loops both increase as the temperature decreases from 20°C to −40°C, indicating an increase in the dynamic stiffness and damping for both the viscous and friction elements. Figure 6(a) also shows that the dynamic stiffness of the friction force is higher than that of the viscous force at both temperatures. However, their energy dissipation remains comparable at 20°C. When the temperature drops to −40°C, the viscous force consumes more energy than the friction force. The changes in overall dynamic properties with temperature are illustrated in Figure 6(b). The hysteresis loop exhibits obvious sharp corners in shape at a higher temperature because the friction force is dominant. However, as the temperature decreases, the viscous force becomes more significant, resulting in a more elliptical shape of the hysteresis loop at lower temperatures. The slope of the loop and its surrounded area both increase as the temperature decreases, with particularly pronounced variations observed when the temperature drops to −40°C. Thus, lowering the temperature leads to an increase in the stiffness and damping and changes the dominant branch from the friction force to viscous force.

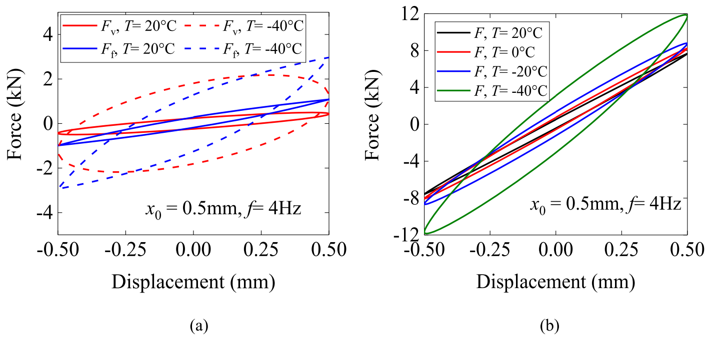

Figure 6. Predicted hysteresis loops for harmonic excitations at different temperatures: (a) hysteresis loops for the viscous and friction forces; (b) hysteresis loops for the total force.

To identify the predominant element under distinct scenarios, the contributions to the dynamic properties from the viscous and friction branches are compared. The stiffness ratio R_K and energy ratio R_E are proposed and expressed as:

$$R_K = \frac{K_{\mathrm{dv}}}{K_{\mathrm{df}}},\ R_E = \frac{E_{\mathrm{v}}}{E_{\mathrm{f}}} \tag{30}$$

where K_{dv} is the dynamic stiffness resulting from the viscous force. When the viscous branch contributes more to the overall dynamic properties, the values of R_K and R_E are larger than 1.

Figure 7 illustrates the variations of R_K and R_E with frequency and amplitude, considering two different temperatures. It is clearly shown that the temperature exerts a strong influence on R_K and R_E, both of which increase when the temperature decreases from 20°C to −40°C. At 20°C, R_K and $R_E$are less than 1 under most scenarios, indicating that the amplitude dependence is more significant than the frequency dependence. Conversely, R_K and R_E are mostly greater than 1 at −40°C, meaning that the viscous element contributes more to the overall properties. Additionally, R_K exhibits larger values with increasing frequency and amplitude at both temperatures, since K_{dv} increases with the frequency, while K_{df} decreases as the amplitude increases. R_E shows distinct trends at different temperatures. At 20°C, it tends to have a larger value with small amplitudes and is insensitive to the frequency. However, at −40°C, it is dominated by the frequency, with higher frequencies resulting in larger values.

In summary, the investigated SARJ exhibits distinct dynamic properties under different scenarios. Conducting vehicle dynamics simulations can prioritise the dominant element of the nonlinear rubber model to reduce the computational effort. For instance, the representation of the friction force should be given priority at higher temperatures, particularly when the SARJ deforms at a low frequency and small amplitude. As the temperature decreases, the frequency dependence of the SARJ becomes more significant, so the viscous force should be accurately represented when investigating low-temperature dynamic performances of vehicles, particularly under displacement excitations with high frequency and large amplitude.

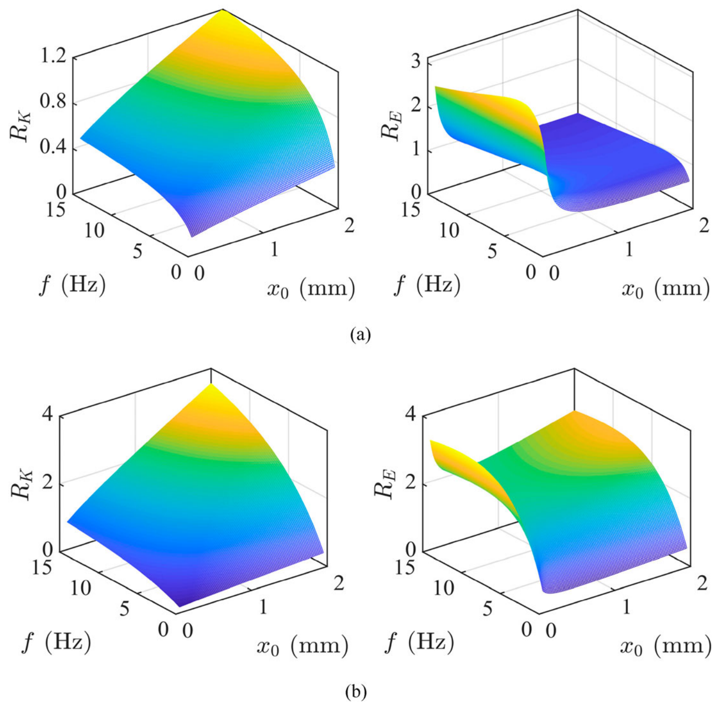

Figure 7. Ratios characterising the contributions from the viscous and friction elements at different temperatures: (a) 20°C; (b) −40°C.

5. Vehicle dynamics simulation

5.1. Dynamic model of the high-speed vehicle

A multi-body dynamic model of a high-speed train is developed in the simulation software SIMPACK considering detailed suspensions. The vehicle model consists of one carbody, two bogie frames, four wheelsets, and eight axle box swing arms. All these components have six degrees of freedom except for the swing arms which only consider a rotation around the wheelset axle. The vehicle contains two stages of suspensions, which are modelled as simplified force elements while fully considering their nonlinear properties. The main parameters of the vehicle model can be found in the Appendix. The track irregularity power spectrum measured in the Wuhan-Guangzhou mainline is used for the following dynamics simulations.

5.2. Implementation of the nonlinear rubber spring model

Since our focus lies on the radial dynamic behaviour of the SARJ, the nonlinear rubber model is applied in its radial direction, and its axial direction is still modelled by the KV model. As expounded in section 2.1, the numerical calculation of the fractional derivative Zener model requires the displacement and force history of the last N_t equidistant time steps. However, the multibody simulation environment is based on the integration algorithm with variable step size, such as the adaptive solver SODASRT2 in SIMPACK

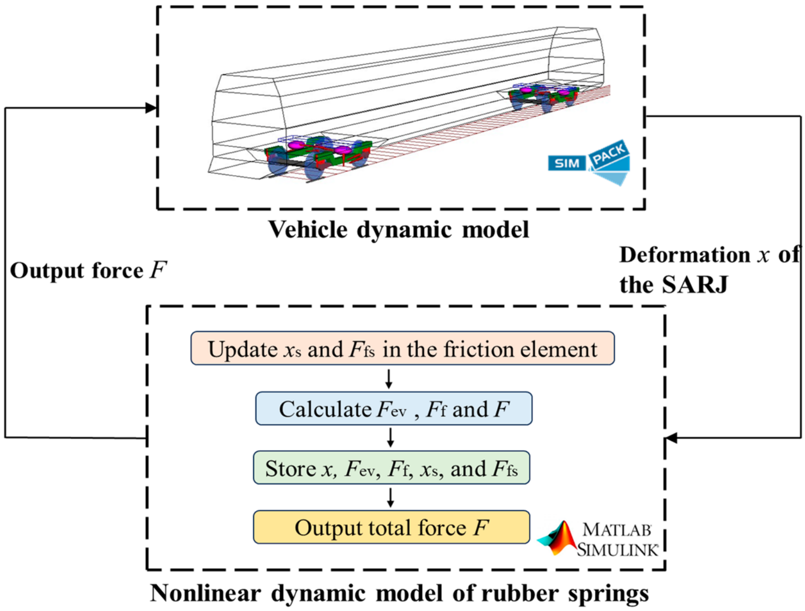

Figure 8. Co-simulation of the vehicle dynamic model and nonlinear dynamic model of the SARJ.

[35], which may result in repeated calls with successively decreasing step sizes until the desired tolerance for a next calculation can be satisfied. Additionally, updating the reference state in Berg's friction model needs to retrieve the displacements of two previous time steps to determine whether the velocity direction changes [18]. This requires data storage as well. To this end, the nonlinear rubber spring model is integrated into the full vehicle dynamic model through a co-simulation interface, as shown in Figure 8.

In the co-simulation, the full vehicle dynamics simulation is performed in SIMPACK, while the nonlinear dynamic model of the SARJ is conducted in MATLAB/Simulink. The vehicle dynamic model outputs the deformations x of the eight SARJs to their corresponding rubber spring models so as to calculate the output forces F, which are then passed back to the vehicle dynamic model for the next calculation. The two dynamic models exchange their results with a constant time step of 1×10^{-3} s. In the dynamic model of the SARJ, the deformation velocity direction is first checked, and the reference state (x_s, F_{fs}) in the friction element will be updated to the displacement and friction force of the last time step if the velocity direction changes. The friction force F_f is then calculated according to Equation (16). Next, the displacement and viscoelastic force of the last 200 time steps are used to calculate the viscoelastic force F_{ev} at the present step, which is combined with F_f to obtain the total force F. It is important to note that x, F_{ev}, F_f, x_s, and F_{fs} must be stored for calculating the next time step.

5.3. *Influence of the dynamic properties of the SARJ*

For investigating the influence of the nonlinear dynamic properties of the SARJ on the dynamic response of the high-speed train, a series of calculations are designed and listed

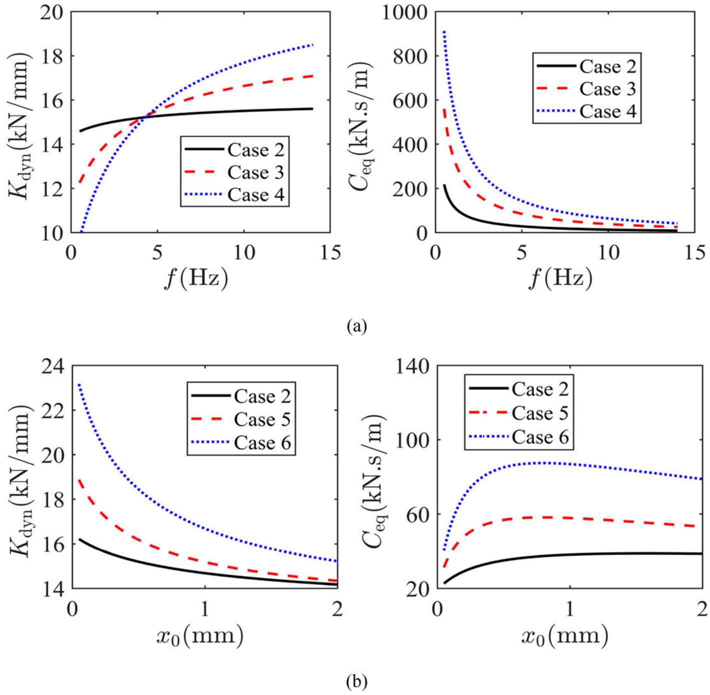

Figure 9. Nonlinear dynamic properties in different cases: (a) frequency dependence; (b) amplitude dependence.

in Table 2. Case 1 is a basic case, in which the traditional KV model is adopted. Its constant stiffness and damping are set to the measurements close to the static test results, namely 14 kN/mm and 243 kN·s/m, respectively, obtained with $f = 0.5$ Hz, $x_0 = 1$ mm, and $T = 20$°C. Case 2 represents the dynamic properties of the SARJ at a temperature of 20°C. Comparing the dynamic simulation results between Cases 1 and 2 can explore the influence of the overall dynamic properties. Cases 2, 3, and 4 are designed to investigate the influence of the frequency dependence. Reducing K_0 and increasing K_∞ yield more significant frequency-dependent dynamic properties, exhibiting a smaller dynamic stiffness at lower frequencies and a larger stiffness at higher frequencies, as shown in Figure 9(a). Cases 2, 5, and 6 explore the effect of the amplitude dependence of the SARJ; their corresponding dynamic stiffnesses increase successively by decreasing x_2 or increasing F_{fmax}, as depicted in Figure 9(b). The effect of the temperature dependence is also investigated by comparing Cases 2, 7, 8, and 9.

Given that the radius of curved tracks on main lines is large for Chinese high-speed railways [36], the vehicle dynamics simulations are conducted on tangent tracks at a speed of 350 km/h. The dynamic behaviour of the SARJ is dependent on the hunting motion of high-speed trains, which is significantly influenced by wheel-rail contact geometries. Therefore, the following simulations consider both the new wheel profile (NWP) and worn wheel profile (WWP), corresponding to wheel-rail contact equivalent conicities of 0.04 and 0.32, respectively. As the equivalent conicity increases, the vehicle hunting motion becomes more severe, resulting in larger working amplitudes and higher frequencies for the SARJ.

Table 2. Calculation cases with various dynamic properties of the SARJ.

		Fractional derivative Zener model				Berg's friction model	
Case	Temperature (°C)	K_0 (kN/mm)	K_∞ (kN/mm)	τ (s)	α	x_2 (mm)	F_{fmax} (kN)
1	20	–	–	–	–	–	–
2	20	12.29	14.01	0.043	0.659	1.41	4.57
3	20	9	17	0.043	0.659	1.41	4.57
4	20	5.5	20	0.043	0.659	1.41	4.57
5	20	12.29	14.01	0.043	0.659	0.705	4.57
6	20	12.29	14.01	0.043	0.659	0.705	8
7	0	12.31	14.08	0.031	0.796	1.58	7.77
8	−20	12.82	17.98	0.018	0.864	1.09	6.18
9	−40	15.06	27.09	0.015	0.861	0.463	6.86

5.4. Comparison of the KV model and nonlinear dynamic model

Figure 10 illustrates the dynamic responses of the vehicle adopting different dynamic models of the SARJ. It can be observed that the relative deformation of the SARJ is larger in the nonlinear dynamic model. Specifically, in the case of the NWP, the SARJ vibrates with an amplitude of 0.3 mm and a frequency of 1.3 Hz, and these values increase to 1 mm and 7.5 Hz, respectively, in the case of the WWP. Therefore, when adopting the traditional KV model, it is essential to select the stiffness and damping measured under the corresponding excitation amplitude and frequency. However, the dynamic behaviour of the SARJ is unavailable prior to vehicle dynamics simulations. On the contrary, the information is unnecessary for the presented nonlinear model because it accurately represents the dynamic behaviour of the SARJ under various conditions, thus making it suitable for applications in vehicle dynamics simulations.

The wear number, computed as the product of creep forces and corresponding creepages, is widely used for predictions of wheel-rail wear and rolling contact fatigue [37]. It is smoothed by a sliding mean window over a 2 m distance with steps of 0.5 m [38], as shown in Figure 10(b). The WWP generates much larger wear numbers than the NWP. Additionally, it can be found that adopting the KV model produces smaller wear numbers for both wheel profiles, indicating an underestimation of the performance deterioration in wheel-rail wear.

The lateral accelerations on the bogie frame and carbody (CBD) are crucial measurements for assessing the running stability and ride comfort of high-speed trains. Carbody hunting, characterised by carbody swing and deterioration of lateral ride comfort, is prone to occur in the presence of a lower equivalent conicity [39]. On the other hand, a higher equivalent conicity may lead to high-frequency bogie hunting [36], triggering instability alarms and threatening regular operation. Therefore, the lateral carbody acceleration is emphatically investigated in the case of the NWP, while the bogie frame acceleration is investigated for the WWP, as shown in Figure 10(c). The carbody experiences reduced vibrations in the frequency range of 0–4 Hz when using the nonlinear rubber spring model, but the vibration amplitude is larger than that in the KV model as the frequency exceeds 4 Hz. The lateral Sperling indexes for the nonlinear model and KV model are 2.19 and 2.28, respectively. The spectrum of the bogie frame acceleration demonstrates its peak at 7–8 Hz in the case of the WWP. The acceleration amplitude is significantly underestimated in the KV model at frequencies higher than 7 Hz. After being processed by a bandpass filter with

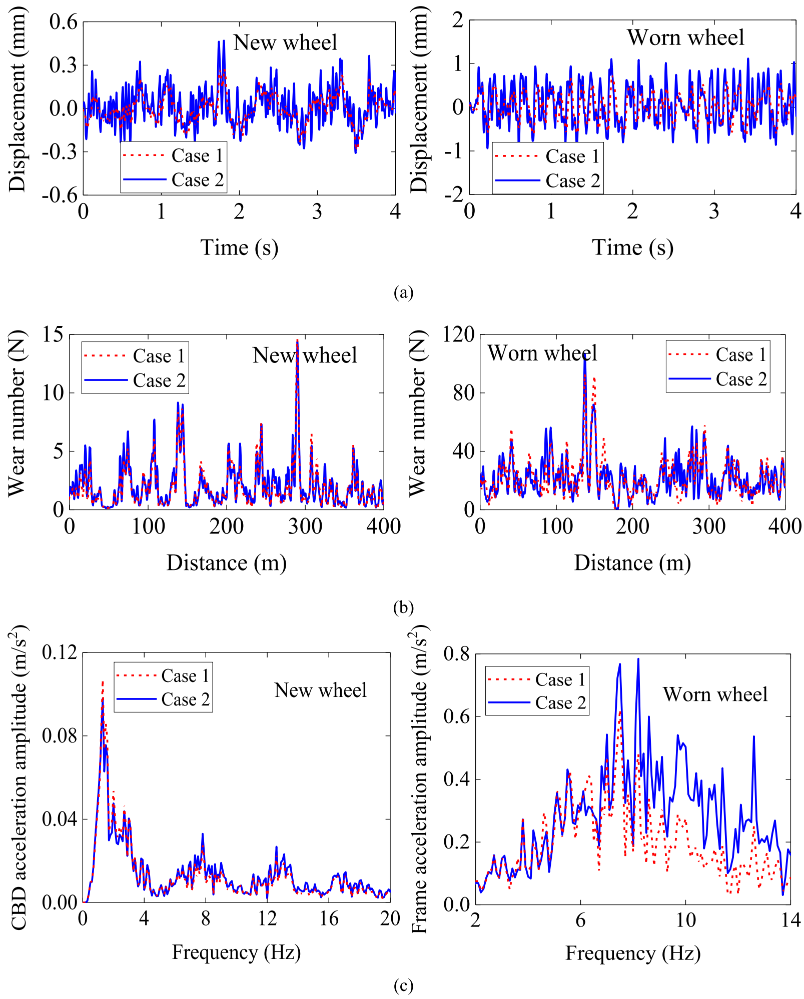

Figure 10. Dynamic responses of the high-speed train with new wheel (left) and worn wheel (right) profiles: (a) relative longitudinal displacement of the SARJ; (b) wear number of the leading wheelset; (c) frequency spectrum of the lateral acceleration on the carbody or bogie frame.

a frequency band of 0.5–10 Hz according to GB/T 5599 [38], the root mean square (RMS) of the lateral bogie frame acceleration in the time domain is 2.2 and 2.5 m/s^2 for the KV model and nonlinear model, respectively.

The nonlinear critical speed of the vehicle is determined by using the decreasing speed method, which yields the most conservative critical speed among several assessment methods [40]. The wheelset starts a limit cycle motion from the beginning due to an initial disturbance, followed by a continuous reduction in speed when running on an ideal straight track. The speed at which the wheelset vibration subsides is regarded as the critical speed. Figure 11 shows the lateral amplitude of the wheelset with the WWP. The wheelset vibration abruptly stops with decreasing speed, indicating a subcritical Hopf bifurcation type of bogie hunting. The nonlinear critical speed shows significant variations in different rubber models, with the nonlinear model giving 533 km/h and the KV model giving

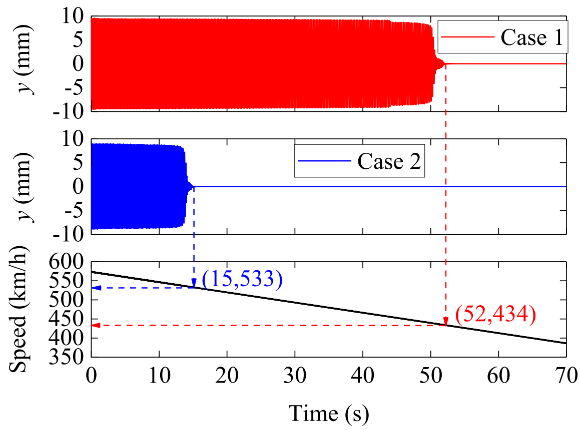

Figure 11. Lateral amplitude of the wheelset with decreasing speed.

Table 3. Nonlinear critical speeds in different cases (km/h).

	Case 1	Case 2	Case 3	Case 4	Case 5	Case 6	Case 7	Case 8	Case 9
New wheel	531	490	485	482	488	477	489	482	445
Worn wheel	434	533	506	479	530	517	530	506	469

434 km/h. However, for the NWP, the nonlinear rubber model produces a lower critical speed, as presented in Table 3. It can be drawn that using the traditional KV model can result in a great deviation in determining the vehicle's critical speed.

5.4.1. Effect of the frequency dependence

To investigate the effect of the frequency dependence of the SARJ, the dynamic performances of the vehicle simulated in Cases 2, 3, and 4 are compared in Figure 12. Changing the frequency dependence has a distinct effect on the dynamic performances when different wheel profiles are considered. In the case of the NWP, which leads to a low working frequency of the SARJ, Case 2 shows the smallest wear number and Sperling index, with the lateral bogie frame acceleration similar to that in the other two cases. With the WWP, the dynamic performances of the vehicle mainly depend on the higher-frequency dynamic properties of the SARJ. The wear number and bogie frame acceleration achieve their smallest values in Case 4, and the Sperling index shows a slight variation with different frequency dependence. In addition, more significant frequency dependence can lead to a lower critical speed for both wheel profiles, as listed in Table 3.

On the whole, amplifying the frequency-dependent dynamic properties of the SARJ improves the dynamic performances of the vehicle in later operation stages but worsen those in early operation stages. Furthermore, although a hydraulic-damping-integrated bush showing significant frequency-dependent stiffness has been applied to swing arms [28,29], with the aim of settling the trade-off between curving performance and vehicle stability, it may not be suitable for the high-speed train investigated in this study. The main concern for the vehicle is its running stability at various wheel-rail contact geometries [41], and amplifying the frequency dependence can worsen that at lower equivalent conicities.

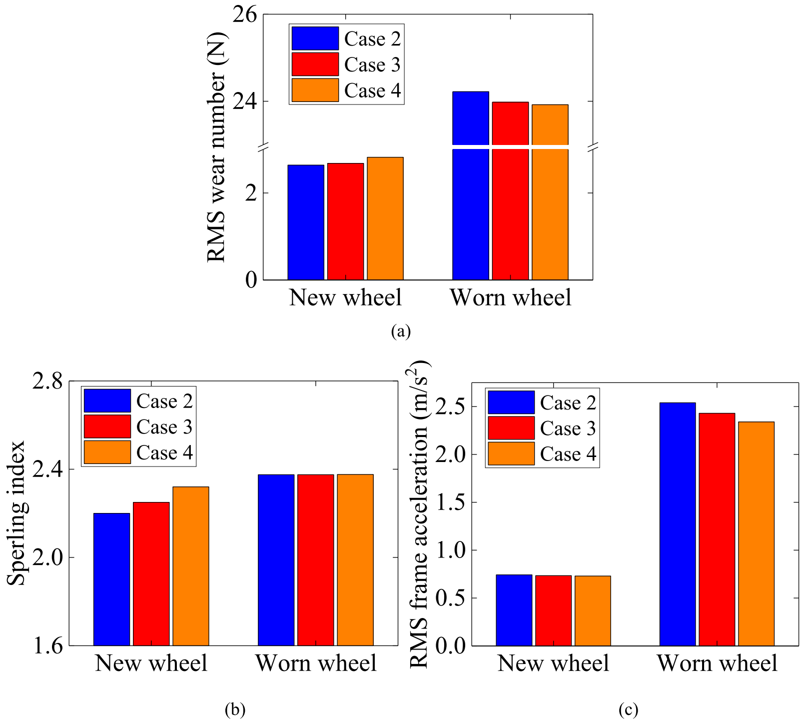

Figure 12. Dynamic performances of the high-speed train in Cases 2, 3, and 4: (a) RMS of the wear number; (b) Sperling index; (c) RMS of the lateral bogie frame acceleration.

5.4.2. Effect of the amplitude dependence

Figure 13 illustrates the dynamic performances of the vehicle using different amplitude dependence of the SARJ. It can be observed that changing the amplitude dependence has a similar effect on the dynamic performances. Enhancing the frictional effect by decreasing x_2 or increasing F_{fmax} leads to a decrease in all three performance indexes under the WWP condition but an increase in the wear number and Sperling index under the NWP condition. Additionally, the critical speed is reduced slightly with increasing frictional stiffness and damping.

5.4.3. Effect of the temperature dependence

In actual operation environments, the ambient temperature varies year-round. Thus, it is essential to analyse the effect of the temperature-dependent dynamic properties of the SARJ on vehicle dynamics. Figure 14 illustrates the dynamic performances of the vehicle at temperatures of 20°C (Case 2), 0°C (Case 7), −20°C (Case 8), and −40°C (Case 9). Lowering the temperature also leads to the performance index variations similar to those observed when amplifying the frequency dependence. Temperatures above −20°C have a limited influence on the dynamic performances of the vehicle, whereas a temperature of −40°C significantly affects them because the dynamic properties of the SARJ have changed greatly. When the temperature drops from 20°C to −40°C, the RMS of the wear number and Sperling index increase by 48% and 13%, respectively, for the NWP, and the RMS of

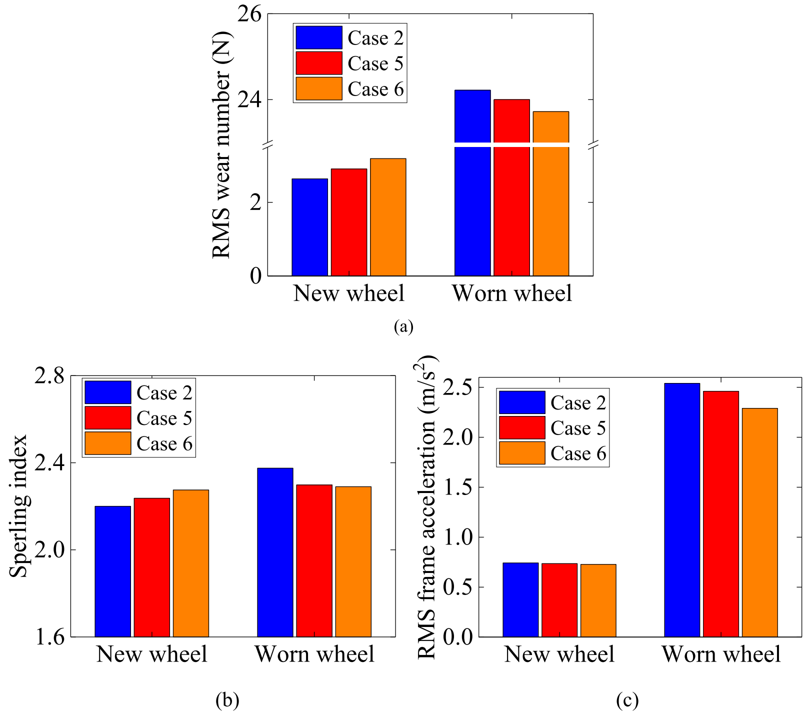

Figure 13. Dynamic performances of the high-speed train in Cases 2, 5, and 6: (a) RMS of the wear number; (b) Sperling index; (c) RMS of the lateral bogie frame acceleration.

the lateral bogie frame acceleration decreases by 24% for the WWP. Moreover, as the temperature decreases, the critical speed continues to decrease, leading to a critical speed of 445 km/h for the NWP and 469 km/h for the WWP at −40°C.

Figure 15 shows the frequency spectrum of the lateral acceleration on the carbody and bogie frame. As the temperature drops from 20°C to −40°C, the carbody acceleration amplitude at the dominant frequency of 1.3 Hz is dramatically amplified in the case of the NWP, resulting in a Sperling index of 2.48. This value approaches the limit of 2.5 defined for the excellent ride comfort level, which is required during regular operation of high-speed trains [38]. Therefore, during the early stage of a wheel reprofiling cycle, the lateral ride comfort of the vehicle deserves significant attention while operating at lower temperatures. In contrast, as the temperature decreases to −40°C, the bogie frame acceleration is significantly attenuated at frequencies higher than 6 Hz under the WWP condition. The running stability of the vehicle can be considered improved from the perspective of assessing the frame acceleration, although its critical speed determined by the decreasing speed method is reduced.

6. Conclusions

This study investigates the frequency-, amplitude-, and temperature-dependent dynamic properties of a swing arm rubber joint (SARJ) in the radial direction by introducing a nonlinear rubber spring model, in which the fractional derivative Zener model represents the

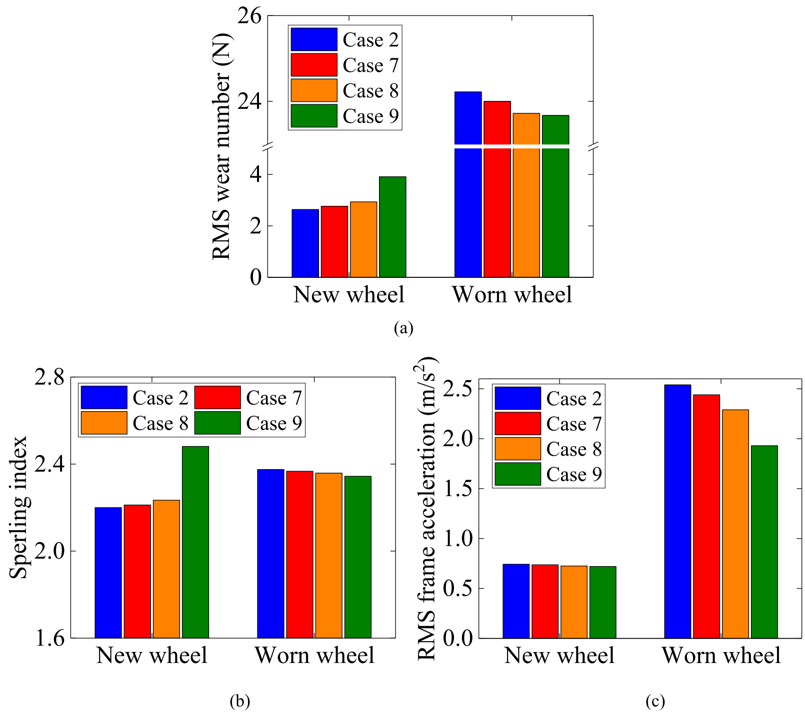

Figure 14. Dynamic performances of the high-speed train in Cases 2, 7, 8, and 9: (a) RMS of the wear number; (b) Sperling index; (c) RMS of the lateral bogie frame acceleration.

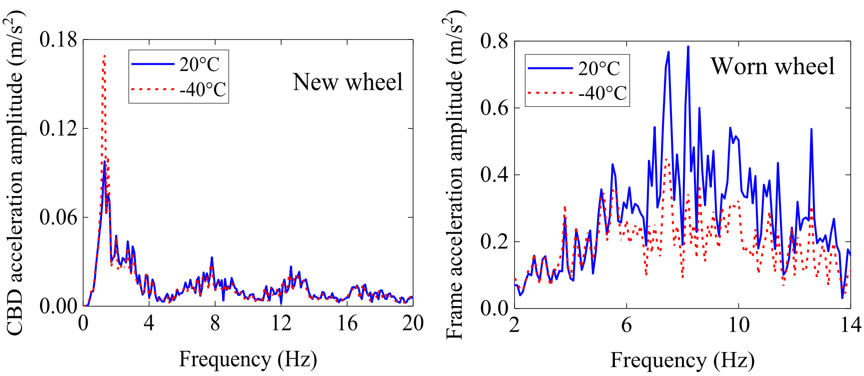

Figure 15. Frequency spectrum of the lateral acceleration on the carbody and bogie frame.

viscoelastic behaviour, and Berg's friction model accounts for the friction behaviour. Referring to the measurements of the SARJ, the model parameters are identified through an optimisation-based method. Then, the nonlinear model is simulated to detail the dynamic properties of the SARJ and integrated into a vehicle dynamic model to investigate the effects of the nonlinear properties on the dynamic behaviour of high-speed trains. The following conclusions can be drawn:

(1) The simulated dynamic stiffness and equivalent damping of the nonlinear model show good agreement with the measurements of the SARJ, particularly at a higher temperature. The dynamic stiffness increases with increasing frequency or decreasing amplitude and temperature, whereas the equivalent damping increases as the frequency and temperature decrease.
(2) The temperature has a significant influence on the frequency and amplitude dependence. Both of them are enhanced as the temperature decreases. Moreover, at lower temperatures, the viscous effect of the SARJ is more significant than the frictional effect, while the reverse is true at higher temperatures.
(3) The dynamic responses of the vehicle obtained with the SARJ described by the nonlinear model and traditional Kelvin–Voigt (KV) model show significant differences, since the KV model cannot capture the SARJ's nonlinear dynamic properties. The effects of the nonlinear properties on the dynamic performance of the vehicle are investigated considering the variation in wheel profiles. Under the new wheel profile condition, enhancing the frequency and amplitude dependence can deteriorate the lateral Sperling index and wear number. However, this improves the lateral bogie frame acceleration and wear number under the worn wheel profile condition. Furthermore, enhancing the frequency and amplitude dependence leads to a decrease in the critical speed, which is determined by the decreasing speed method. The similar features also can be found when lowering the temperature. The lateral ride comfort requires special attention at a temperature of −40°C under the new wheel profile condition, since it deteriorates significantly and approaches the limit for the excellent ride comfort level.

Disclosure statement

No potential conflict of interest was reported by the author(s).

Funding

The material in this paper is based on work supported by the National Natural Science Foundation of China [grant numbers 52372403; U2268211], the Natural Science Foundation of Sichuan Province [grant numbers 2022NSFSC0034; 2022NSFSC1901], and the National Railway Group Science and Technology Program [grant number N2023J071].

ORCID

Yuan Yao http://orcid.org/0000-0003-2279-7463

References

[1] Iwnicki S, Spiryagin M, Cole C, et al. Handbook of railway vehicle dynamics. 2nd ed. Boca Raton (FL): CRC Press; 2020.
[2] Evans J, Berg M. Challenges in simulation of rail vehicle dynamics. Veh Syst Dyn. 2009;47(8):1023–1048. doi:10.1080/00423110903071674
[3] Babitsky VI, Veprik AM. Universal bumpered vibration isolator for severe environment. J Sound Vib. 1998;218(2):269–292. doi:10.1006/jsvi.1998.1832
[4] Sun DW, Zhen ZG, Zhang GY, et al. Modeling and parameter identification of amplitude- and frequency-dependent rubber isolator. J Cent South Univ Technol. 2011;18(3):672–678. doi:10.1007/s11771-011-0746-y

[5] Luo Y, Liu Y, Yin HP. Numerical investigation of nonlinear properties of a rubber absorber in rail fastening systems. Int J Mech Sci. 2013;69:107–113. doi:10.1016/j.ijmecsci.2013.01.034
[6] Pintado P, Ramiro C, Berg M, et al. On the mechanical behavior of rubber springs for high speed rail vehicles. J Vib Control. 2018;24(20):4676–4688. doi:10.1177/1077546317732206
[7] Yarmohamadi H, Berbyuk V. Computational model of conventional engine mounts for commercial vehicles: validation and application. Veh Syst Dyn. 2011;49(5):761–787. doi:10.1080/00423111003770439
[8] Polach O. Modelling of rubber components using estimated parameters. International Symposium on Dynamics of Vehicle on Road and Tracks, IAVSD; 2015.
[9] Bagley R, Torvik P. Fractional Calculus-A different approach to the analysis of viscoelastically damped structures. AIAA J. 1983;21(5):741–748. doi:10.2514/3.8142
[10] Sjoberg M, Kari L. Non-linear behavior of a rubber isolator system using fractional derivatives. Veh Syst Dyn. 2002;37(3):217–236. doi:10.1076/vesd.37.3.217.3532
[11] Sedlaczek K, Dronka S, Rauh J. Advanced modular modelling of rubber bushings for vehicle simulations. Veh Syst Dyn. 2011;49(5):741–759. doi:10.1080/00423111003739806
[12] Shi HL, Wu PB. A nonlinear rubber spring model containing fractional derivatives for use in railroad vehicle dynamic analysis. Proc Inst Mech Eng Part F-J Rail Rapid Transit. 2016;230(7):1745–1759. doi:10.1177/0954409715614871
[13] Yang F, Wang P, Wei K, et al. Investigation on nonlinear and fractional derivative Zener model of coupled vehicle-track system. Veh Syst Dyn. 2020;58(6):864–889. doi:10.1080/00423114.2019.1602273
[14] Wei K, Zhao ZM, Ren JJ, et al. High-speed vehicle-slab track coupled vibration analysis of the viscoelastic-plastic dynamic properties of rail pads under different preloads and temperatures. Veh Syst Dyn. 2021;59(2):171–202. doi:10.1080/00423114.2019.1673444
[15] Xiao HY, Xu CZ, Wang RB, et al. A nonlinear model and parameter identification method for rubber isolators under shock excitation in underwater vehicles. J Mar Sci Eng. 2021;9(11):1282. doi:10.3390/jmse9111282
[16] Shi YP, Li JJ, Wang Y, et al. A full range experimental study of amplitude- and frequency-dependent characteristics of rubber springs. Polymers. 2022;14(21):4662. doi:10.3390/polym14214662
[17] Berg M. Model for rubber springs in the dynamic analysis of rail vehicles. Proc Inst Mech Eng Part F-J Rail Rapid Transit. 1997;211(2):95–108. doi:10.1243/0954409971530941
[18] Berg M. A non-linear rubber spring model for rail vehicle dynamic analysis. Veh Syst Dyn. 1998;30(3–4):197–212. doi:10.1080/00423119808969447
[19] Yang J. Study on dynamic characteristics of rubber spring. [Master thesis]. Southwest Jiaotong University; 2015 [In Chinese].
[20] Luo R, Shi HL, Guo JY, et al. A nonlinear rubber spring model for the dynamics simulation of a high-speed train. Veh Syst Dyn. 2020;58(9):1367–1384. doi:10.1080/00423114.2019.1624788
[21] Sohn JH, Lee SK, Yoo WS. Hybrid neural network bushing model for vehicle dynamics simulation. J Mech Sci Technol. 2008;22(12):2365–2374. doi:10.1007/s12206-008-0712-2
[22] Dai LC, Chi MR, Xu CB, et al. A hybrid neural network model based modelling methodology for the rubber bushing. Veh Syst Dyn. 2022;60(9):2941–2962. doi:10.1080/00423114.2021.1933090
[23] Shi HL, Zeng J, Qu S. Linear stability analysis of a high-speed rail vehicle concerning suspension parameters variation and active control. Veh Syst Dyn. 2022. doi:10.1080/00423114.2022.2147086
[24] Guan QH, Du X, Wen ZF, et al. Vibration characteristics of bogie hunting motion based on root loci curves. Acta Mech Sin. 2022;38(2):521447. doi:10.1007/s10409-021-09025-x
[25] Wu XW, Chi MR. Parameters study of Hopf bifurcation in railway vehicle system. J Comput Nonlin Dyn. 2015;10(3):0310123.
[26] Polach O, Vuitton J. Which parameters determine the type of bogie hunting bifurcation? International Symposium on Dynamics of Vehicle on Road and Tracks. IAVSD; 2019.
[27] Song ZK, Wang H, Hu XY, et al. Study on influence of stiffness of service nodal point of rotary arm on operation vehicle dynamics. J China Railw Soc [In Chinese]. 2020;42(4):35–42.

[28] Lewis TD, Jiang JZ, Neild SA, et al. Using an inerter-based suspension to improve both passenger comfort and track wear in railway vehicles. Veh Syst Dyn. 2020;58(3):472–493. doi:10.1080/00423114.2019.1589535
[29] Qu C, Li Y, Jiang JZ, et al. Reducing wheel-rail surface damage by incorporating hydraulic damping in the bogie primary suspension. Veh Syst Dyn. 2022. doi:10.1080/00423114.2022.2092012
[30] Pritz T. Analysis of four-parameter fractional derivative model of real solid material. J Sound Vib. 1996;195(1):103–115. doi:10.1006/jsvi.1996.0406
[31] Pritz T. Five parameter fractional derivative model for polymeric damping materials. J Sound Vib. 2003;265:935–952. doi:10.1016/S0022-460X(02)01530-4
[32] Das S. Functional fractional calculus. Heidelberg: Springer; 2011.
[33] Alonso A, Gil-Negrete N, Nieto J, et al. Development of a rubber component model suitable for being implemented in railway dynamic simulation programs. J Sound Vib. 2013;332(12):3032–3048. doi:10.1016/j.jsv.2013.01.002
[34] Dai LC. Study on service performance of key suspension components of railway vehicles. [PhD thesis]. Southwest Jiaotong University; 2022 [In Chinese].
[35] SIMPACK. 2018 documentation. France: Dassault Systemes Simulia Corp; 2017.
[36] Shi HL, Wang JB, Wu PB, et al. Field measurements of the evolution of wheel wear and vehicle dynamics for high-speed trains. Veh Syst Dyn. 2018;56(8):1187–1206. doi:10.1080/00423114.2017.1406963
[37] Dirks B, Enblom R. Prediction model for wheel profile wear and rolling contact fatigue. Wear. 2011;271(1–2):210–217. doi:10.1016/j.wear.2010.10.028
[38] GB/T 5599-2019. Specification for dynamic performance assessment and testing verification of rolling stock. China: National Railway Administration; 2019.
[39] Li YX, Chi MR, Guo ZT, et al. An abnormal carbody swaying of intercity EMU train caused by low wheel–rail equivalent conicity and damping force unloading of yaw damper. Railway Eng Sci. 2023. doi:10.1007/s40534-022-00295-w
[40] Polach O. On non-linear methods of bogie stability assessment using computer simulations. Proc Inst Mech Eng Part F-J Rail Rapid Transit. 2006;220(1):13–27. doi:10.1243/095440905X33251
[41] Yao Y, Chen XW, Li H, et al. Suspension parameters design for robust and adaptive lateral stability of high-speed train. Veh Syst Dyn. 2023;61(4):943–967. doi:10.1080/00423114.2022.2062012

Appendix

Table A1. Main parameters of the high-speed vehicle.

Parameter	Value	Unit
Carbody mass	36630	kg
Bogie frame mass	2547	kg
wheelset mass	1560	kg
Axle box swing arm mass	203	kg
Inertia moment of carbody about longitudinal/lateral/vertical axis	118/1775/1670	$t{\cdot}m^2$
Inertia moment of bogie frame about longitudinal/lateral/vertical axis	1924/1012/2811	$kg{\cdot}m^2$
Inertia moment of wheelset about longitudinal/lateral/vertical axis	811/122/811	$kg{\cdot}m^2$
Inertia moment of axle box swing arm about longitudinal/lateral/vertical axis	7/14/9	$kg{\cdot}m^2$
Primary vertical damping	10	kN·s/m
Secondary longitudinal stiffness	0.167	kN/mm
Secondary lateral stiffness	0.167	kN/mm
Secondary vertical stiffness	0.278	kN/mm
Secondary lateral damping	40	kN·s/m
Damping of yaw damper	2450	kN·s/m
Series stiffness of yaw damper	8.82	kN/mm
Stiffness of anti-roll bar	1	MN.m/rad
Wheel base	2.5	m
Length between bogie centres	17.8	m
Wheel rolling radius	0.43	m
Operation speed	350	km/h